Trench filling by ionized metal physical vapor deposition

Junqing Lu[a] and Mark J. Kushner[b]
University of Illinois, 1406 W. Green Street, Urbana, Illinois 61801

(Received 25 January 2001; accepted 16 July 2001)

Ionized metal physical vapor deposition (IMPVD) is a process in which sputtered metal atoms from a magnetron target are ionized by a secondary plasma, accelerated into the substrate, and deposited with moderately anisotropic fluxes. To investigate these processes, an integrated plasma equipment and feature scale model was developed to simulate the sputtering of metal atoms, their transport in IMPVD reactors, and their deposition into trenches. The model self-consistently predicts the magnitude and distributions (energy and angle) of the depositing metal flux and the profiles of metal deposits in trenches. The predicted profiles agree with experimentally observed trends. The results indicate that the ionization fraction of the depositing metal flux is the critical factor in trench filling. Formation of voids occurs when the ionization fraction of the depositing metal flux is too low or the aspect ratio of the trench is too large. As the aspect ratio of the trench increases, the ionization fraction required for complete trench filling also increases. To increase the ionization fraction, high pressure, low magnetron power and high inductively coupled plasma power are the desired operating conditions. To the degree that the ionization fraction and the ion flux angular distribution vary as a function of radius on the substrate, so will the trench filling properties. This is particularly true near the edge of the wafer where fluxes may be asymmetric. © *2001 American Vacuum Society.* [DOI: 10.1116/1.1399318]

I. INTRODUCTION

As the number of devices per die increases and the critical dimension decreases, the time delay resulting from metal interconnect wiring becomes an increasingly important consideration in optimizing the performance of integrated circuits (ICs). As much as 90% of the signal delay time in the 100 nm generation of ICs will likely be due to the interconnection wiring, while only 10% will be due to the actual device switching.[1,2] Advanced ICs are beginning to use Cu in place of Al as the interconnect metal because the resistance of Cu is 40% lower than Al. As a result, the signal delay time due to the RC time constant for Cu wiring is shorter than that for Al. The shrinking of devices also leads to increasing aspect ratios of the dielectric trenches and vias in the interconnect layer which are backfilled with metal to fabricate the wiring. The state of the art for interconnect wiring is to fully fill the trench and vias using physical vapor deposition (PVD) techniques, or to deposit diffusion barriers and Cu seed layers into high aspect ratio ($>$5:1) trenches and vias using PVD, and fill the remainder of the structure using electrochemical plating.[3]

Ionized metal physical vapor deposition (IMPVD) is being developed as a method to fill these structures or to deposit diffusion barriers and Cu seed layers into high aspect ratio trenches and vias.[4,5] In a typical IMPVD reactor, a dc bias of 100s V applied to a magnetron accelerates ions into the target thereby producing physical sputtering of the metal. A secondary plasma, typically an inductively coupled plasma (ICP), is produced between the target and the substrate by a radio-frequency (rf) driven antenna. The plasma is usually sustained in an inert gas such as Ar at moderate pressures of 10s mTorr to slow the sputtered atoms and ionize them prior to their reaching the substrate. Typical ionization fractions of the metal are 10s percent to as large as 90%. An rf or dc bias may be applied to the substrate to vertically accelerate the metal ions into the wafer. The combination of anisotropic metal ions and isotropic neutral metal atoms results in conformal deposition and prevents pinch-off[5] when filling trenches. (Pinch-off refers to the trench being closed near the top of the feature prior to fully filling thereby producing an internal void.)

Trench filling using IMPVD has been the subject of numerous studies. Hamaguchi and Rossnagel[6] performed experimental and numerical studies of Al IMPVD at 2 kW magnetron power, 1 kW ICP power, 35 mTorr Ar, and -20 V dc bias on the substrate. As the ion-to-neutral ratio of the depositing metal flux was increased from 3:7 to 7:3, the deposition profile transitioned from being pinched-off to completely filled. This work established the scaling law that a higher fraction of ions in the metal flux is beneficial to complete trench filling. As the ion energy was increased from 20 to 120 eV by increasing the substrate bias, the trench profiles transitioned from being completely filled to being pinched-off due to excessive sputtering at the bottom of the trench. (Note that in most IMPVD systems, the metal ion flux is typically a small fraction of the total ion flux, with the balance coming from the buffer gas ions.) Cheng *et al.*[7] used Cu IMPVD to fill trenches of 600 nm width and 1.1 aspect ratio. At 0.3 kW magnetron power, 1.0 kW ICP, and -25 V dc bias on the substrate, pinch-off was observed at 5 mTorr while complete filling was obtained at 40 mTorr.

[a]Department of Mechanical and Industrial Engineering; present address: Novellus Systems, 4000 North First St., San Jose, CA 95134; electronic mail: junqing.Lu@novellus.com
[b]Author to whom correspondence should be addressed; Department of Electrical and Computer Engineering; electronic mail: mjk@uiuc.edu

These results were attributed to the increasing ion-to-neutral ratio of the incident metal flux which is typically obtained as the pressure increases.

Vyvoda *et al.*[8] developed a string-type feature evolution model utilizing reflection and resputtering distributions obtained by molecular dynamics simulations to investigate conformal lining of trenches with an aspect ratio of 5. The simulations were carried out for ion-neutral flux ratios from 1:1 to 7:3, with ion energies from 100 to 175 eV and 90% of the ions being Cu^+. They found that ion assisted mechanisms of Cu transport (such as sputtering) are the dominant means of redistributing copper within the evolving feature. This ion dominance can be a result of high ion energies as well as the higher ion-neutral flux ratios which can be achieved at the bottom of the feature. For example, the Cu thickness at the bottom of the feature decreased (relative to the side walls) with increasing ion energy due to high rates of sputtering.

In this article we present results from a fully integrated modeling study of trench filling using Cu IMPVD. The computational platforms used in this study are the two-dimensional Hybrid Plasma Equipment Model (HPEM)[9] and the Monte Carlo Feature Profile Model (MCFPM).[10] The consequences of pressure, magnetron power, ICP power, and aspect ratio on trench filling were investigated. It was found that the ionization fraction of the incident metal flux is the critical factor for trench filling. Formation of voids occurs when the ionization fraction of the incident metal flux is too low, the precise value being a function of aspect ratio. The critical value is, depending on the reactor conditions, 50% at an aspect ratio of 0.7 and 86% at an aspect ratio of 3.0. The ionization fraction can be increased, to an upper limit of $\approx$90%, by increasing pressure and ICP power, and by decreasing magnetron power. The model will be described in Sec. II, followed by a discussion of predicted gas phase properties from the reactor scale modeling in Sec. III. Trench filling is discussed in Sec. IV. The concluding remarks are in Sec. V.

II. DESCRIPTION OF THE MODEL

The HPEM and the MCFPM have been previously described in detail.[9,10] The HPEM is a modular simulator which iteratively achieves a quasi-steady state solution. The modules used here are the Electromagnetics Module (EMM), the Electron Energy Transport Module (EETM), and the Fluid Kinetics Simulation (FKS). Inductively coupled electric and magnetic fields are computed in EMM. These fields are then used in EETM to solve the electron energy equation for the temperature of bulk electrons and, using Monte Carlo techniques, the trajectories and distribution functions of secondary electrons emitted from the cathode. The electron temperatures and energy distributions are used to compute source rates for electron impact processes and electron transport coefficients. These rates and coefficients are then used in the FKS where continuity, momentum, and energy equations are solved for all heavy particles (neutrals and ions). Poisson's equation is solved for the electric potential throughout the reactor. Sheaths at the target and substrate are resolved using a semianalytic sheath model for both rf and dc sheaths. The sputter transport and heating algorithms, described below, are included in the FKS. Densities and electric fields are then transferred to the EMM and EETM, and the process is repeated until a converged solution is obtained. The gas pressure was held constant at the specified value in the presence of gas heating by throttling the pump rate. The electron motion in radial and axial directions is resolved within each rf period. The electron motion in the azimuthal direction is not resolved in the fluid modules, but is accounted for in the conservation of momentum through use of tensor conductivity in the presence of static magnetic fields. Azimuthal trajectories are explicitly tracked in the Monte Carlo modules. The plasma properties shown here are averaged over several rf periods.

To obtain the energy and angular distributions of reactive species to the substrate, the Plasma Chemistry Monte Carlo Module (PCMCM) was developed for the HPEM. The PCMCM calculates the trajectories of plasma species in the gas phase and their collisions with surfaces. This module was originally a postprocessor to the HPEM. It used volumetric sources of plasma species, time dependent electric fields, and sheath properties exported from the HPEM to obtain the angular and energy distributions of the fluxes using Monte Carlo techniques.[10] The PCMCM functions in a similar manner but also accounts for nonthermal, or inflight fluxes, resulting from sputter sources in addition to the volumetric sources. Sputtered atoms and neutralized ions which are reflected from the target have kinetic energies of several eV. These species are not initially in thermal equilibrium with the buffer gas which has a temperature of $\leqslant$0.3 eV. Under certain process conditions, these energetic particles may not thermalize prior to reaching the wafer. The trajectories and energies of these nonequilibrium particles are already tracked by the sputter algorithms in the FKS. Statistics on the energy and angular distributions of the particles as they strike selected surfaces are collected and passed to the PCMCM.

The operation of the integrated PCMCM is similar to the postprocessor,[10] and so will be briefly described here. The PCMCM is typically executed at the end of the HPEM after species densities, fluxes, and electrical properties have converged. Based on these quantities, a rate of generation of species i as a function of position, $G_i(\vec{r})$ $(\mathrm{cm}^{-3}\,\mathrm{s}^{-1})$, is computed. This generation term accounts for all sources of species i on the right-hand side of reactions in the mechanism. $G_i(\vec{r})$ also includes source functions on surfaces due to, for example, sputtering. In a similar fashion, a consumption rate $C_i(\vec{r})$ $(\mathrm{cm}^{-3}\,\mathrm{s}^{-1})$ is computed based on all reactions containing species i on the left-hand side of reactions in the mechanism. A local elastic collision frequency with each species is also computed. These elastic frequencies are added to the local consumption frequency $C_i(\vec{r})\Delta V(\vec{r})$[$\Delta V(\vec{r})$ is the volume of the computational cell at location $\vec{r}$] to yield a total interaction frequency $\nu_T(\vec{r})$. Null collision techniques are used at each spatial location to provide a reactor wide collision frequency ν_i for each species i.

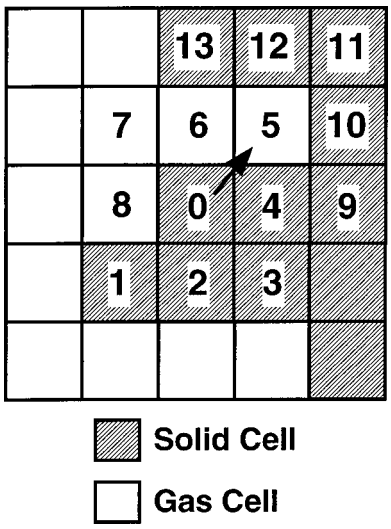

FIG. 1. Schematic of the rectangular mesh used in the MCFPM. One diffusion step is shown, during which solid cell 0 diffuses to location 5.

Pseudoparticles of species i are launched from each computational cell at a time randomly chosen in the rf cycle with a weighting (or total number) proportional to $G_i(\vec{r})\Delta V(\vec{r})$. The velocity is randomly chosen from a Maxwell–Boltzmann distribution having a local temperature $T_i(\vec{r})$ for volumetric sources where the spatial dependent temperature for each species is computed by HPEM. For sputter sources from surfaces, the pseudoparticle velocity is determined by the energy and identity of the incident ion.[8] The trajectories of the pseudoparticles are integrated for the time

$$\Delta t = -\frac{1}{\nu_i}\ln r, \tag{1}$$

where Δt is the time step for movement of the pseudoparticle and r is a random number distributed on (0,1). For ions, acceleration by the local electric field is accounted for. In the case of sputtered species having initial energies of a few eV, additional considerations, such as inflight electron impact excitation, are also accounted for.[11] The time step used to increment the trajectory is limited by the time required to cross a specified fraction of the cell (typically 0.2). For ions, additional constraints are applied including a specified fraction of the rf cycle (typically 0.05), or the time to cross a specified fraction of the sheath width (typically 0.01).

At the end of the time step, Monte Carlo techniques are used to determine if the collision is real or null. If real, another random number is used to determine if the collision is elastic or consuming. If consuming, the particle is removed from the simulation. If elastic, the collision partner is identified using another random number and the velocity of the pseudoparticle is changed appropriately using standard elastic collision techniques. The one exception is for charge exchange collisions which are separately accounted for in the sum of collision frequencies. If an ion undergoes a charge exchange collision its identity is changed to the neutral counterpart and the trajectory is retained. The trajectories are advanced until the pseudoparticles reach the vicinity of a surface. If the surface is chosen as one for which statistics on incident species are desired, ions are then integrated through the sheath, a computationally expensive process. For nonselected surfaces, the particles are removed from the simula-

TABLE I. Surface reaction mechanism for Cu deposition with an Ar buffer gas.

Reaction[a]	Reaction probability[b]	Reference
$Ar^+ + Cu_s \rightarrow Ar_g + Cu_g$	$0.35\frac{\varepsilon-\varepsilon_h}{\varepsilon_r-\varepsilon_t}$	14, c,d
$Ar^+ + SiO_{2s} \rightarrow Ar_g + SiO_{2g}$	$0.10\frac{(\varepsilon-\varepsilon_t)^{1/2}}{(\varepsilon_r-\varepsilon_t)^{1/2}}$	15, c,d
$Cu^+ + Cu_s \rightarrow Cu_g + Cu_g$	$0.35\frac{\varepsilon-\varepsilon_t}{\varepsilon_r-\varepsilon_t}$	14, c,e
$Cu^+ + Cu_s \rightarrow Cu_s + Cu_s$	0.55	e,f
$Cu^+ + Cu_s \rightarrow Cu_g + Cu_s$	0.10	e,f
$Cu^+ + SiO_{2s} \rightarrow Cu_g + SiO_{2g}$	$0.10\frac{(\varepsilon-\varepsilon_t)^{1/2}}{(\varepsilon_r-\varepsilon_t)^{1/2}}$	15, c
$Cu^+ + SiO_{2s} \rightarrow Cu_s + SiO_{2s}$	0.80	e,f
$Cu^+ + SiO_{2s} \rightarrow Cu_s + SiO_{2g}$	0.10	e,f
$Cu_g + Cu_s \rightarrow Cu_s + Cu_s$	0.95	f
$Cu_g + Cu_s \rightarrow Cu_g + Cu_s$	0.05	f
$Cu_g + SiO_{2s} \rightarrow Cu_s + SiO_{2s}$	0.70	f
$Cu_g + SiO_{2s} \rightarrow Cu_g + SiO_{2s}$	0.30	f
$Cu^* + Cu_s \rightarrow Cu_s + Cu_s$	0.95	f
$Cu^* + Cu_s \rightarrow Cu_g + Cu_s$	0.05	f
$Cu^* + SiO_{2s} \rightarrow Cu_s + SiO_{2s}$	0.70	f
$Cu^* + SiO_{2s} \rightarrow Cu_g + SiO_{2s}$	0.30	f

[a]Subscript (s) denotes a surface species. Subscript (g) denotes a gas or plasma species. All ion reactions also apply to hot neutrals and reflected neutrals having high energy.
[b]ε is the ion energy. ε_r (100 eV) is the reference energy. ε_t(45 eV) is the threshold energy for sputtering. For $\varepsilon<\varepsilon_t$, sputtering does not occur.
[c]Sputter yield was derived from the cited reference. The incident angles of the ions are 0°.
[d]Remaining probability is assigned to nonsputtering reflection.
[e]The reaction probabilities for sputtering, deposition, and reflection add to 1 at the reference energy of 100 eV. At other energies, the reflection and sticking coefficients are adjusted to give the total unity probability. The reflection coefficient is increased at low energies and the sticking coefficient is decreased at high energies.
[f]Estimated.

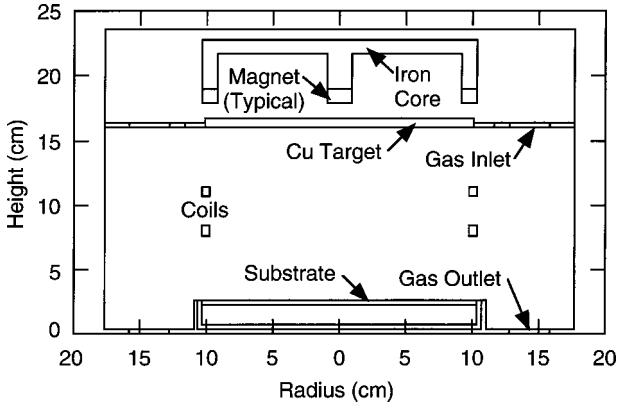

FIG. 2. Schematic of the IMPVD reactor. The reactor has a magnetron on top with a Cu target and coils that are immersed in the plasma.

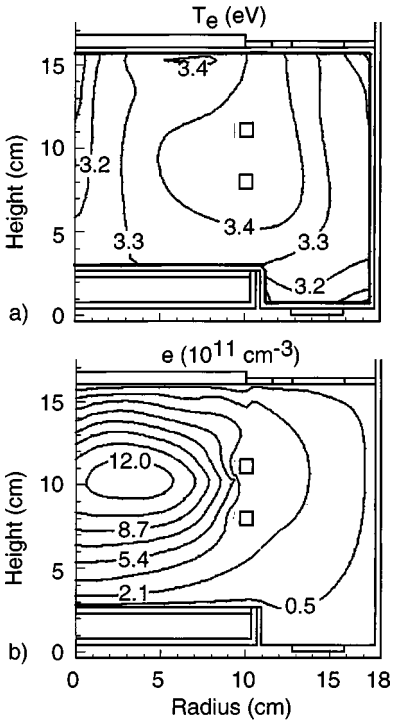

FIG. 3. Electron temperature and density for the base case (40 mTorr, 0.3 kW magnetron, 1.0 kW ICP, and −25 V dc bias on the substrate). (a) electron temperature and (b) electron density. The electron temperature peaks near the sputter track and the coils. The electron density peaks off-axis due the magnetron effect and the ionization source near the coils.

tion. A similar process is followed for the neutrals, except for integration through the sheath.

The MCFPM was first developed to predict etch profiles as a function of position on the wafer using the fluxes and energy and angular distributions produced by HPEM.[10] The MCFPM resolves the trench region on the wafer using a rectilinear mesh with typical spacings of 100s cells for 1.0 μm length. The length of one solid cell represents the width of $<30-40$ atoms. Each cell is assigned a material identity, which may change during the simulation. Gas phase species are represented by pseudoparticles. The solid materials are represented by computational cells. Pseudoparticles are launched from random locations above the trench with energy and angles sampled from the distributions of incident fluxes. The trajectories of these particles are tracked until they hit the solid material. Depending on the gas–solid reaction mechanism, adsorption, etching, sputtering, or deposition occurs, and the identity of the computational cell is changed accordingly.

When initially applied to deposition the MCFPM predicted unphysical dendritic growth due to the line-of-sight algorithm employed for sticking of incident species. A surface diffusion algorithm was therefore added to the MCFPM. In using this algorithm all metal atoms incident onto a specified material are placed into a physical adsorption state. These physisorbed atoms are distinct from the underlying material even if they have the same composition. The physisorbed atoms diffuse on the surface until chemisorbed, at which time they become part of the underlying material.

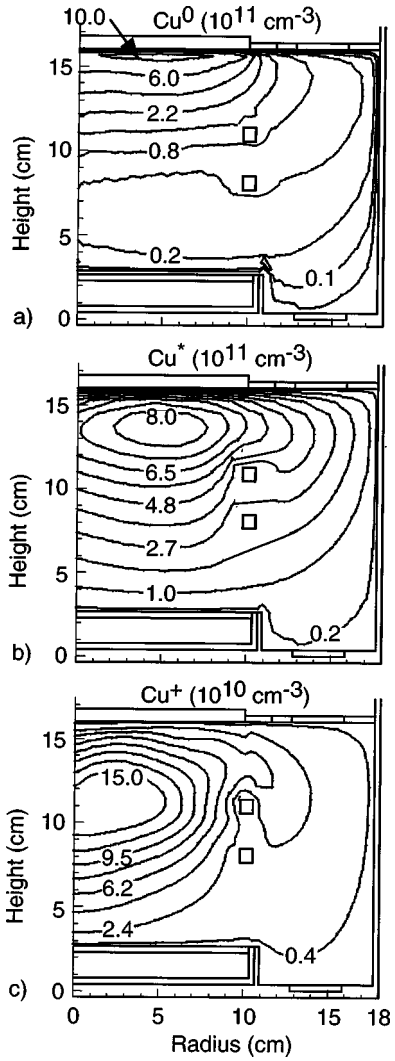

FIG. 4. Cu species densities for the base case. (a) Total Cu^0 (thermal and inflight), (b) Cu*, and (c) Cu^+. The Cu^0 and Cu* densities peak below the sputter track, and Cu^+ peaks near the axis of the reactor.

The diffusion algorithm used here is based on the work of Wei *et al.*[12] for thin film growth. Given that the atom diffuses, the probability that an adsorbed atom at surface site i diffuses to another surface site j is

$$p_{ij}=\frac{\exp\left(-\frac{E_{ij}}{k_B T_s}\right)}{\sum_{k=1}^{m}\exp\left(-\frac{E_{ik}}{k_B T_s}\right)}, \quad E_{ij}=E_j-E_i, \tag{2}$$

where E_{ij} is the activation energy for diffusion from site i to site j, k_B is Boltzmann's constant, and T_s is the substrate temperature, which was maintained at 393 K for this study.[7] E_j and E_i are the potentials for the surface site at the new and the old locations. The sum is over all possible diffusion sites. For the rectilinear mesh used in this study, there are eight such sites, as shown in Fig. 1. Note that E_i and E_j are usually negative because the potentials are generally attractive for the interparticle spacing of interest. When employed on a numerical mesh, as opposed to an atom-by-atom basis

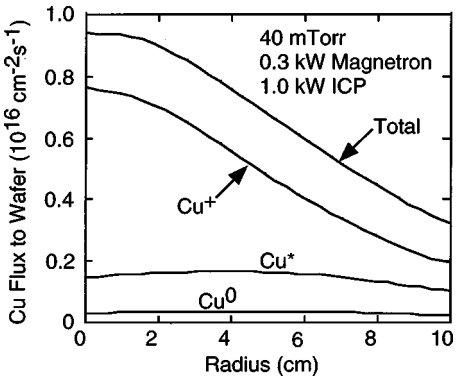

FIG. 5. Cu fluxes to the substrate for the base case. The majority of the Cu flux is Cu^+, and the majority of Cu neutrals is Cu*.

as in molecular dynamics simulation, each numerical cell is analogous to a pseudoparticle. The potentials can be therefore modeled by atomic functions as in a molecular dynamics approach.

Using this approach, the potentials E_j and E_i are the sum of potentials between the numerical cell of interest and its neighboring numerical cells. For example, for the adsorbed atoms represented by cell 0 in Fig. 1 to diffuse to location 5, the contributing cells to E_0 are cells 1–4. The contributing cells to E_5 are cells 4 and 9–13. Note that the adsorbed cell can only diffuse to the immediate neighboring cells 1–8. Diffusion to more remote locations in one step is prohibited.

The potential between any two given cells i and j, Φ_{ij}, is based on the atomic Morse potential

$$\Phi_{ij}=\Phi_0\left\{\exp\left(-2\,\frac{r_{ij}-r_0}{a_0}\right)-2\exp\left(-\frac{r_{ij}-r_0}{a_0}\right)\right\}, \tag{3}$$

where r_{ij} is the distance between the center of the cells. Morse potentials are commonly used to represent atom-to-atom potentials so that r_0 and a_0 typically have atomic scale lengths (approximately the equilibrium distance), and Φ_0 is $\leqslant 1$ eV. In analogy, r_0 and a_0 have mesh scale lengths. We chose $r_0=7.5$ nm and $a_0=22.5$ nm, and set $\Phi_0=0.3$ eV commensurate with typical metal atom potentials.[12]

The probabilities for diffusion to all possible locations are summed and normalized to 1, as shown in Eq. (2). An adsorbed cell cannot diffuse to a location already occupied by another solid cell and so that probability is zero. A random number is generated to determine the location to which diffusion then occurs. Based on the chosen value of E_{ij}, a rejection algorithm is used to determine whether a cell actually diffuses or is chemisorbed and bonds to the underlying material at its present site. The jump frequency ν to the new site j is

$$\nu=-\nu_{ij}\ln(r), \tag{4}$$

where

$$\nu_{ij}=\nu_0\exp\left(-\frac{E_{ij}}{k_BT_s}\right) \tag{5}$$

and

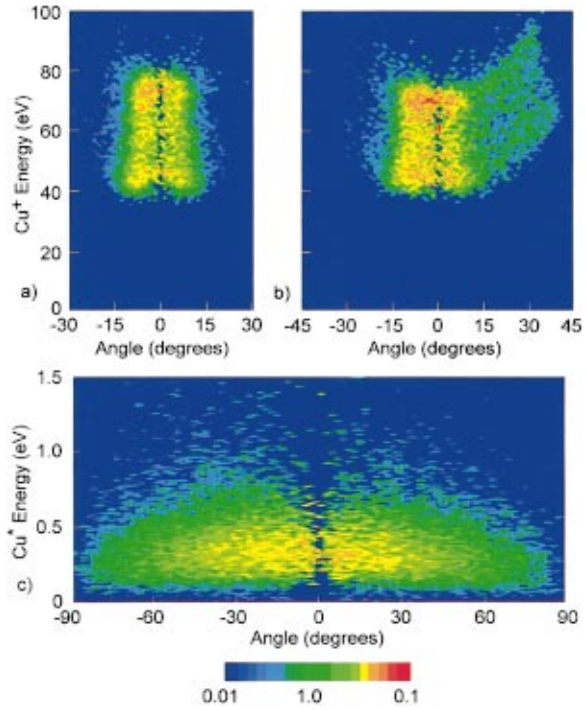

FIG. 6. Energy and angular distributions for incident Cu^+ and Cu* for the base case. (a) Cu^+ distributions at the center of the substrate (typical across the substrate), (b) Cu^+ distributions at the edge of the substrate, and (c) Cu* distributions. The energy spread for Cu^+ is mostly due to plasma potential oscillation caused by the rf coil voltage.

$$\nu_0=2k_BT_s/h, \tag{6}$$

where h is Planck's constant. At 393 K, ν_0 is $1.6\times10^{12}\,s^{-1}$. If $\nu\geqslant\nu_t$, where ν_t is a specified threshold value, the diffusion step is taken. If $\nu<\nu_t$, the cell chemisorbs. The threshold frequency ν_t is the only adjustable parameter in the diffusion algorithm and was chosen to be $10^9\,s^{-1}$, as will be discussed later.

The volumetric plasma chemistry has been previously described in detail.[13] The majority of the reactions belong to either electron-impact reactions or charge-exchange reactions. The electron-argon chemistry includes electron impact excitation of Ar from ground state to excited states $4s$ and $4p$ (which are lumped into Ar*) and electron impact ionization (from Ar ground state and Ar*). The electron-copper chemistry includes electron impact excitation of Cu from ground state $[^2S_{1/2}]$ to higher excited states $[^2D_{5/2}]$, $[^2D_{3/2}]$, $[^2P_{1/2}]$, $[^2P_{3/2}]$ (which are lumped into Cu*), and electron impact ionization (from Cu ground state and Cu*). The Cu* is quenched by collisions with Cu, Cu*, and Ar. The Ar* reacts with Ar* to produce Ar^+ and with Cu or Cu* to produce Cu^+ through Penning processes. Charge exchange reactions play an important role in generating fast neutral fluxes to the target and ionizing Cu atoms before they reaching the substrate. The reaction rates for charge exchange are large, approximately $10^{-9}\,cm^{-3}\,s^{-1}$. As the precise value of the Ar^+–Cu charge-exchange rate coefficient is not known, a sensitivity study was performed. Changes in copper species densities are less than 10% for a 50% change in the charge-

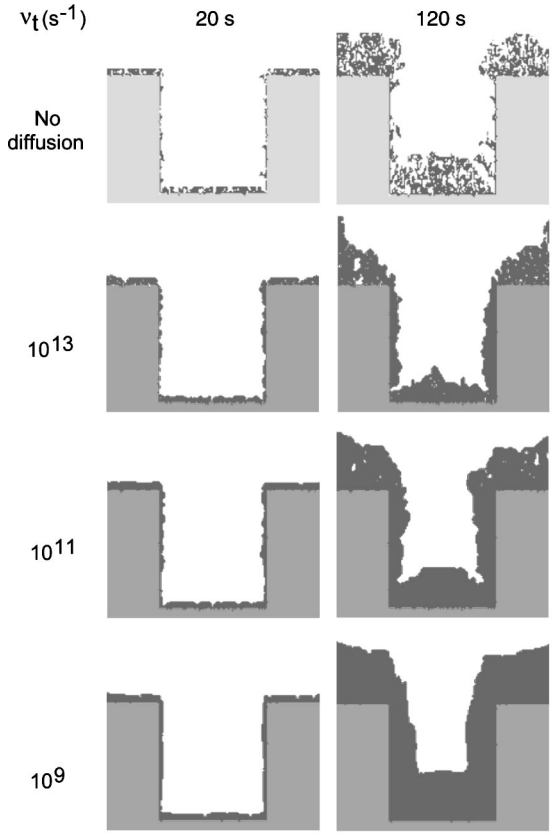

FIG. 7. Trench filling profiles with and without the diffusion algorithm for the base case. With diffusion, Cu species deposit compactly and conformally. Results are shown for different values of ν_t, the threshold for chemisorption.

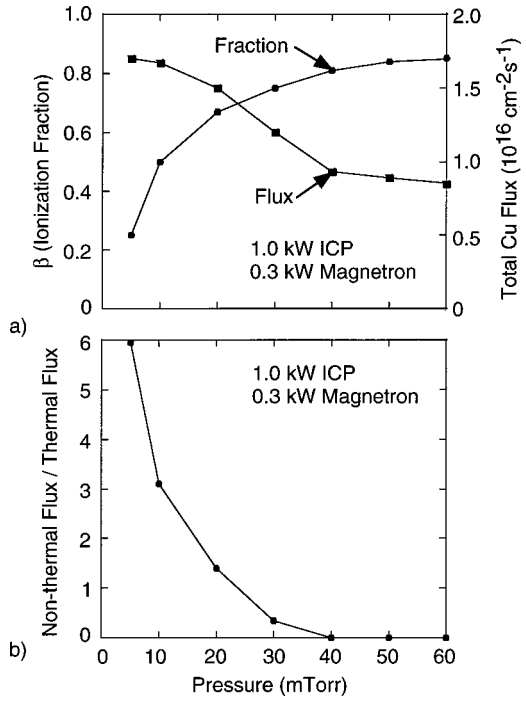

FIG. 8. Incident Cu flux properties as a function of pressure for 0.3 kW magnetron, 1.0 kW ICP, and −25 V dc bias on the substrate: (a) Ionization fraction and total Cu flux to the substrate. (b) Ratio of nonthermal to thermal Cu neutral flux. β is the ionization fraction of the incident metal atom flux. β increases with pressure while the magnitudes of the total flux and the nonthermal flux decrease.

exchange reaction rates. The charge-exchange reactions also include resonant exchange among the Ar species or the Cu species which contributes to gas heating as well as the nonresonant exchange between Ar^+ and Cu species.

The surface reaction mechanism implemented in the MCFPM is shown in Table I. For Ar^+ incident on Cu or SiO_2, sputtering occurs for an ion energy greater than the threshold energy ε_t. The Ar^+ is neutralized at the surface and reflected as a hot neutral. For incident Cu^+, deposition occurs in addition to sputtering and reflection. Note that hot neutrals are treated in the same manner as ions with the same energy. Thermal Cu ground state and Cu* [nominally the Cu($^2D_{5/2}$) state] deposit and reflect only. The sticking probability of Cu and Cu* on SiO_2 surfaces is estimated to be 0.7, less than the sticking probability of 0.95 on Cu surfaces. The sputter yield algorithm listed in Table I is for ions incident at normal angle. For non-normal incidence, the yield is modified based on data from molecular dynamics studies.[16,17] These yields are generally maximum at near 45° and approach zero near grazing angle. The proportion of ions which are reflected specularly is increased from zero to unity from 70° to 90°.[17]

III. REACTOR SCALE PROPERTIES

In order to obtain self-consistent magnitudes of the depositing fluxes, the HPEM was used to model the plasma species densities throughout the reactor. The reactor of interest is similar to that studied by Cheng *et al.*,[6] as shown in Fig. 2. The diameters of the target and the rf induction coils are both 20 cm. The upper turn of the two-turn coil (separation 3 cm) is 5 cm from the target. The diameter of the substrate is 21 cm. The distance between the target and the substrate is 13 cm. The base case operating conditions are 1.0 kW ICP power, 0.3 kW magnetron power, 40 mTorr Ar buffer gas, and 150 sccm gas flow. The magnetic field is 250 G at a radius of 5 cm at the surface of the target. The secondary emission coefficient for electron production by ions was 0.15. The rf voltage on the inductive coil was specified to be 100 V, which is typical for this type of discharge. Due to the small size of the coil, a large dc bias of −90 V is generated to balance currents in what appears to be an asymmetric discharge. This rf and dc bias combination results in about 20 V of rf oscillation in the plasma potential, in good agreement with the measurements of Suzuki *et al.*[18]

The predicted electron temperature and density are shown in Fig. 3. The electron temperature ranges from 3.1 to 3.4 eV and peaks near the coil due to the large ICP power deposition and below the sputter track on the target due to secondary electron heating. The small variation in electron temperature is due to the large electron thermal conductivity. The electron density peaks at $1.2\times10^{12}\,\mathrm{cm}^{-3}$, off axis, 6 cm below the target. This off-center maximum is caused by the off-center ICP power deposition and the magnetron effect.

The predicted Cu species densities are shown in Fig. 4.

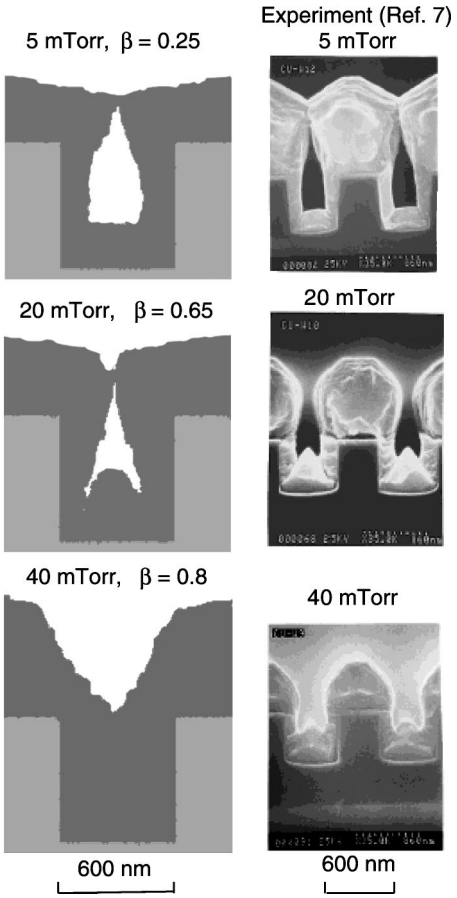

FIG. 9. Trench filling profiles as a function of pressure for 0.3 kW magnetron, 1.0 kW ICP, and −25 V dc bias on the substrate. The size of the void decreases with increasing pressure due to an increase in ionization fraction β. The trench is completely filled at 40 mTorr.

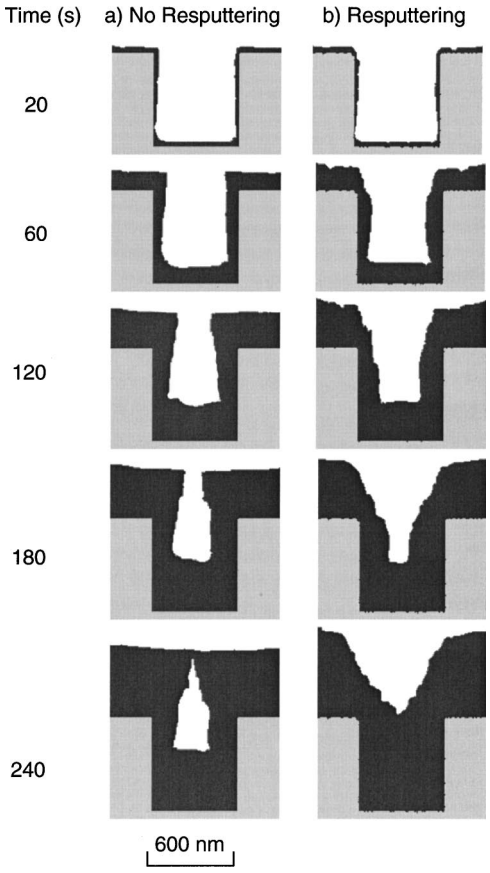

FIG. 10. Trench filling as a function of time for the base case. (a) Without resputtering. (b) With resputtering. Resputtering is essential to keeping the mouth of the trench clear.

The total ground state Cu density, denoted by Cu^0 (sum of thermal and nonthermal or inflight species), peaks below the target at $1\times10^{12}\,cm^{-3}$ and diminishes to $1\times10^{10}\,cm^{-3}$ above the wafer. This decrease in density is due in part to the diverging trajectories of the Cu^0 atoms originating from the sputter track. Because Cu* is metastable and has a low excitation energy of 1.4 eV, the Cu* density can be larger than Cu^0 density. The Cu* density ranges from $8\times10^{11}\,cm^{-3}$ at 2 cm below the target to $2\times10^{10}\,cm^{-3}$ above the wafer. The Cu^+ density peaks at 5 cm below the target, about 2 cm off the reactor axis. This off-axis peak is largely due to the magnetron effect and the off-axis ionization source by ICP power.

The Cu fluxes to the wafer are shown in Fig. 5. The total Cu flux to wafer (neutral and ion) ranges from $9.4\times10^{15}\,cm^{-2}\,s^{-1}$ at the center to $3.2\times10^{15}\,cm^{-2}\,s^{-1}$ at the edge. With the ion flux being center peaked, the Cu* and Cu^0 fluxes are more uniform than the Cu^+ flux and are about 1.5×10^{15} and $3.0\times10^{14}\,cm^{-2}\,s^{-1}$ across the wafer, respectively. As a result, the ionization fraction of the incident flux ranges from 80% at the center to 60% at the edge. At this relatively high pressure of 40 mTorr, the majority of the incident flux consists of ions. The majority of the neutral Cu flux is Cu*, consistent with the Cu species densities in Fig. 3. Note that no attempt was made to make the total flux uniform.

The energy and angular distributions of Cu^+ and Cu* incident on the substrate are shown in Fig. 6. Cu^+ distributions typical of the central portions of the wafer (to within about 1 cm of the edge) are shown in Fig. 6(a). The majority of Cu^+ ions have energies between 40 and 80 eV. The spread in Cu^+ energy is primarily due to the oscillation in the plasma potential caused by the rf voltage on the coil, and to a lesser extent, collisional broadening in the presheath. The time averaged sheath potential is 60 V (including the −25 V of applied dc bias) with an rf amplitude variation in the plasma potential of 20 V, producing the range of ion energy from 40 to 80 eV. The Cu^+ flux distributions near the edge of the wafer are shown in Fig. 6(b). The angular distribution is asymmetric, due to the radial electric fields at the edge of the wafer which produce ions skewed >15° from the normal. The majority of Cu* has energies between 0.1 and 0.7 eV, with the average being around 0.3 eV. This relatively high Cu* energy is a reflection of the gas heating produced by energetic sputtered and ion reflection neutrals and charge exchange neutrals. The majority of incident Cu^+ is within 15° of the normal, while the Cu* is diffusively distributed between 0° and 90°. The distributions in Fig. 6 are the raw statistics collected divided by solid angle $\sin\theta\cdot d\theta$ to provide

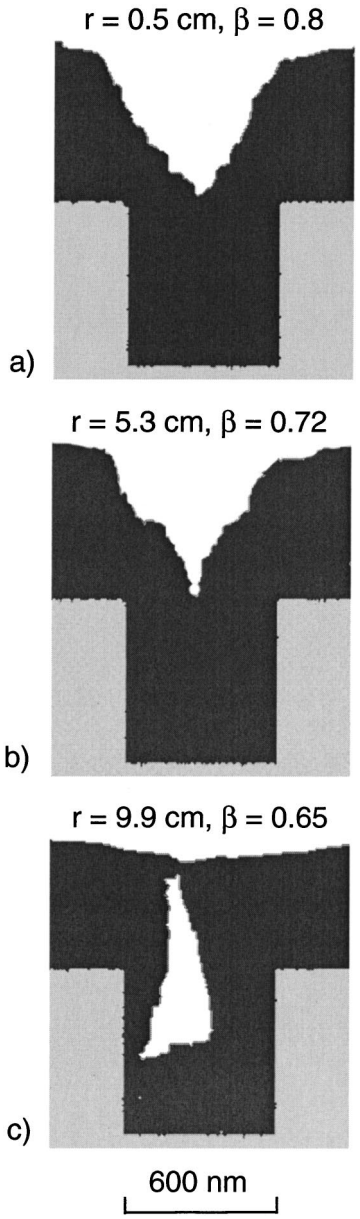

FIG. 11. Deposition profiles at three radial locations on the wafer for the base case conditions. (a) 0.5, (b) 5.3, and (c) 9.9 cm. The asymmetric filling at $r=9.9$ cm is due to the asymmetric distributions of the incident Cu^+.

the angular distribution. Theoretically, there should be a maximum at 0°. However, due to the finiteness of the mesh upon which these statistics are collected, the maximum occurs at a small angle away from the normal.

IV. TRENCH FILLING

The incident fluxes and their angular and energy distributions were used by MCFPM to investigate trench filling. Profiles as a function of the adjustable parameter ν_t, the threshold hopping frequency, are shown in Fig. 7. Without surface diffusion (ν_t=infinity), the predicted profiles are unphysically porous and nonconformal. For $\nu_t=10^{13}\,s^{-1}$, only atoms with positive E_{ij} have frequencies large enough to diffuse, and so the conformity improves but the deposits were

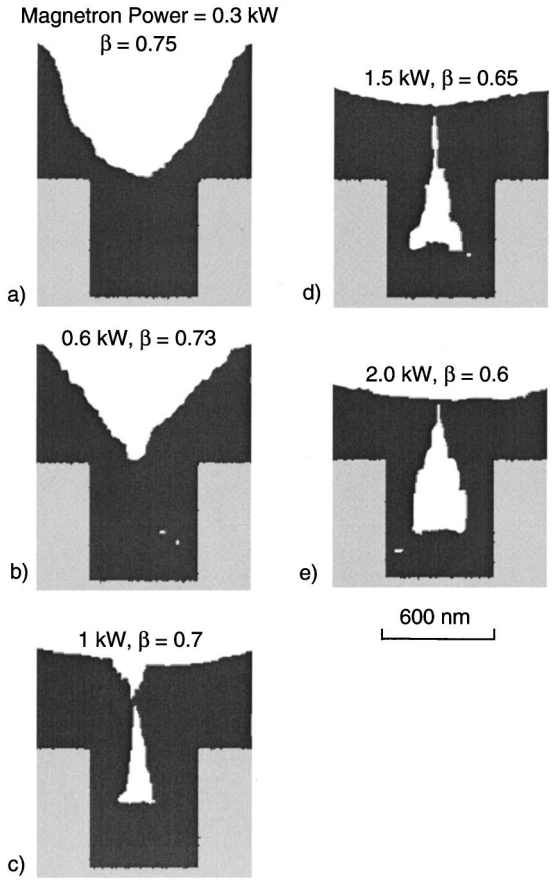

FIG. 12. Deposition profiles at 30 mTorr, 1 kW ICP, and −30 V bias on the wafer for magnetron powers of (a) 0.3 kW, (b) 0.6 kW, (c) 1 kW, (d) 1.5 kW, and (e) 2 kW. Voids form at high magnetron power (>1 kW) due to there being a low ionization fraction of the incident Cu flux.

still porous, especially at the top of the trench. As ν_t decreases, a larger number of atoms diffuse, the deposits become more compact, and the agreement with the appearance of the experimental profile improves.[7] Hence $\nu_t=10^9\,s^{-1}$ was used for the rest of the study.

As pressure increases, the mean free path for Cu neutrals (2 cm at 20 mTorr, 1000 K) decreases. A larger fraction of Cu neutrals are thermalized and have a higher probability of undergoing ionizing collisions as the pressure increases. Hence the ionization fraction of the incident metal fluxes increases with pressure, as shown in Fig. 8(a). At pressures above 40 mTorr, the ionization fraction starts to saturate at about 0.85. The magnitude of the total Cu fluxes are $1.7\times10^{16}\,cm^{-2}\,s^{-1}$ at 5 mTorr and about $0.8\times10^{16}\,cm^{-2}\,s^{-1}$ at 40 mTorr [also shown in Fig. 8(a)]. This decrease is due to the reduction in the incident nonthermal flux and the loss of Cu neutrals to other surfaces as a consequence of increased diffusion and backscattering into the target. For example, the ratio of the nonthermal to thermal Cu fluxes decreases from about 3 at 10 mTorr to only 0.3 at 30 mTorr, as shown in Fig. 8(b). To characterize the incident fluxes, we use β, which is the ionization fraction of the incident Cu fluxes, defined as [Cu^+ flux/(total Cu flux)].

The consequences of pressure on trench filling are shown

in Fig. 9. A void in the profile occurs at low pressure (5 mTorr) which is progressively filled with increasing pressure. At the relatively high pressure of 40 mTorr the trench is completely filled. The simulated profiles generally agree with the experiments by Cheng *et al.*[7] In particular, the model was able to predict the pinch-off at 5 mTorr and the microtrenching at 20 mTorr, as shown in Fig. 9. The mircotrenching is due to the specular reflection and focusing of the high energy ions from the sidewall into the corners at the bottom. The model does not capture the faceting at the top of the deposition. This is likely due to there being some disagreement for the ion angular distribution or the sputtering probability as a function of angle. The model predictions indicate that the critical factor that determines the degree of filling or pinch-off is β, which increases from 0.25 at 5 mTorr to 0.8 at 40 mTorr. The drawback for increasing pressure is that the deposition rate decreases, as shown in Fig. 8(a).

The reasons for pinch-off at a low fraction of incident ions are twofold. The first is the diffuse angular distribution of the incident neutral flux that results in the neutrals depositing preferentially at the top of the trench due to the larger solid angle of the plasma viewed from those locations. The second is that there is less sputtering of the resulting overhang deposits due to there being fewer ions. For example, the consequences of resputtering (due to both Ar^+ and Cu^+) of the Cu deposits were examined by comparing the profiles with and without resputtering in Fig. 10. Results at 40 mTorr are shown as a time sequence during the fill. Without resputtering, the overhang deposits grow faster than the bottom of the trench, due to the larger solid angle of incident species available at the top of the trench. This faster growth of the overhang deposits eventually seals the trench and results in pinch-off. When resputtering is allowed, the overhang deposits are progressively eroded to keep the opening clear. As a result more Cu flux arrives at the bottom to fill the trench, as shown in Fig. 10(b). The species that does most of the sputtering is Ar^+, which outnumbers the Cu^+ by a ratio of 7.5:1. The total Cu flux to the substrate is about $10^{16}\,cm^{-2}\,s^{-1}$, at best producing fill of a 600 nm trench in about 2 min. The predicted filling time is about 4 min due to sputter and reflection losses.

The predicted deposition profiles at three radial locations on the wafer are shown in Fig. 11. At $r=0.5$ cm (near the center of the wafer) and $r=5.3$ cm, the trenches were filled due to the large values of β at those locations (0.8 and 0.72, respectively). The symmetric distributions of the incident ions, which are well represented by Fig. 6(a), contribute to this filling. At $r=9.9$ cm (at the edge of the wafer), there is a void and the fill is asymmetric. The void is produced by the smaller β of 0.65. The asymmetry is produced by the asymmetric ion energy and angular distribution shown in Fig. 6(b).

The effect of magnetron power on trench filling at 30 mTorr is shown in Fig. 12. At powers of $\leqslant$0.6 kW, the trench is completely filled. However, as the magnetron power is increased to 1 kW and higher, pinch-off occurs.

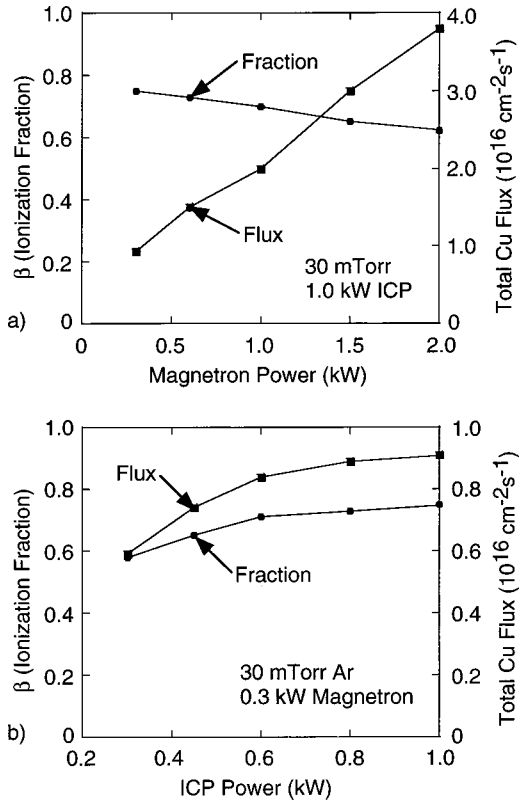

FIG. 13. Ionization fraction and total Cu flux to the substrate. (a) As a function of magnetron power at 30 mTorr, 1.0 kW ICP, and −30 V dc bias on the substrate. (b) As a function of ICP power for 30 mTorr, 0.3 kW magnetron, and −30 V dc bias on the substrate. The ionization fraction of the incident Cu fluxes decreases slowly with magnetron power while the magnitude of the total flux linearly increases. Both the ionization fraction of the incident Cu fluxes and the magnitude of the total flux increase with ICP power.

This trend is largely due to a decrease in the ionization fraction of the incident metal flux from 0.75 to 0.6 as the magnetron power is increased from 0.3 to 2 kW, as shown in Fig. 13(a). As the magnetron power increases, the incident ion flux to target and the target bias increase, and more Cu atoms are sputtered into the plasma resulting in a nearly linear increase in the flux to the substrate. Since the resulting rates of total ionization of the sputtered Cu atoms are largely set by the ICP power, which is held constant while the total Cu inventory increases, the ionization fraction of the Cu flux decreases. As the magnetron power increases, the gas temperature increases due to sputter heating,[9,19,20] resulting in a more rarefaction and fewer thermalizing collisions. For example, the nonthermal fraction of neutral Cu flux to the substrate increases from almost zero at 0.3 kW to about 0.1 at 2 kW. To maintain the same ionization fraction while increasing the magnetron power, the ICP power must be increased to compensate for the larger Cu inventory. Although void-free fillings are obtained at low magnetron power, the incident metal flux is also lower, as shown in Fig. 13(a).

The consequences of ICP power on trench filling while holding the magnetron power constant are shown in Fig. 14. The ionization fraction and magnitude of the incident flux are shown in Fig. 13(b). As the ICP power increases from

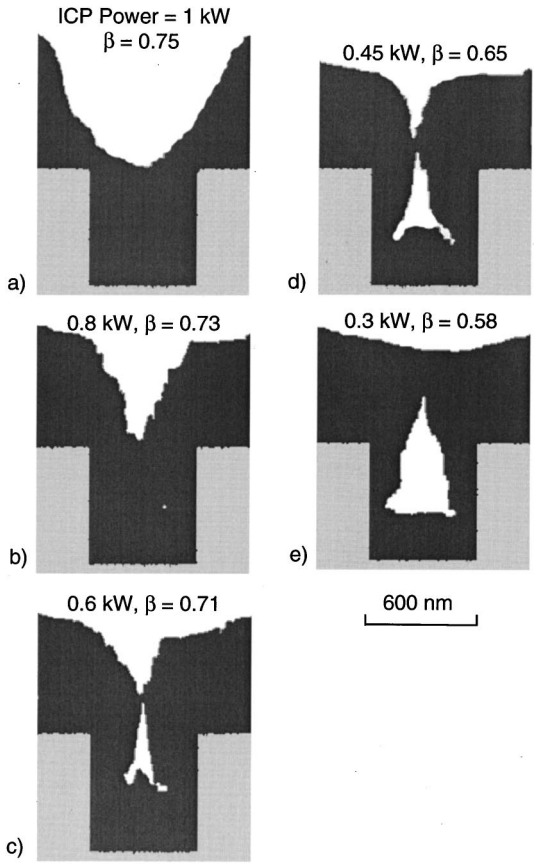

FIG. 14. Deposition profiles at 30 mTorr, 0.3 kW magnetron, and −30 V bias on the substrate as a function of ICP power. (a) 1.0 kW, (b) 0.8 kW, (c) 0.6 kW, (d) 0.45 kW, and (e) 0.3 kW. Voids form at low ICP power (<0.8 kW) due to a lower value of β.

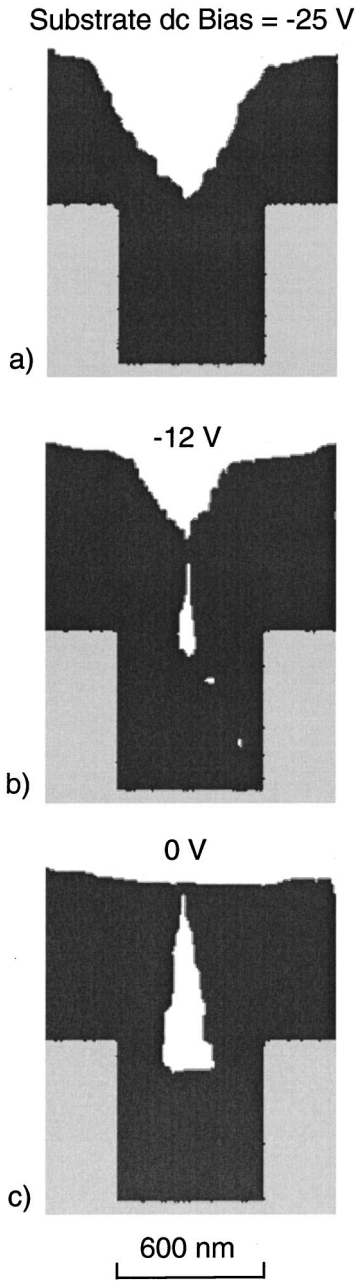

FIG. 15. Deposition profiles at 40 mTorr, 0.3 kW magnetron, 1 kW ICP as a function of substrate dc bias. (a) −25 V, (b) −12 V, and (c) 0 V. Pinch-off occurs at less negative biases due to less resputtering and a broader angular distribution of the incident ions.

0.3 to 1.0 kW at 30 mTorr for a fixed magnetron power of 0.3 kW, the void obtained at low power is progressively filled. As ICP power increases, the rate of Cu ionization increases, and consequently the ionization fraction of the incident metal flux increases from 0.58 at 0.3 kW to 0.75 at 1.0 kW, as shown in Fig. 13(b). This trend is facilitated by an increase in the reactor averaged electron density from $1.0\times10^{11}\,\mathrm{cm}^{-3}$ at 0.3 kW to $3.1\times10^{11}\,\mathrm{cm}^{-3}$ at 1.0 kW. Moreover, the incident Cu fluxes also increase with ICP power from $0.6\times10^{16}\,\mathrm{cm}^{-2}\,\mathrm{s}^{-1}$ at 0.3 kW ICP to $0.9\times10^{16}\,\mathrm{cm}^{-2}\,\mathrm{s}^{-1}$ at 1.0 kW ICP. This increase in incident flux tends to saturate as the ICP power increases due to rarefaction caused by gas heating.[9,19,20] The increase in flux is due to a larger contribution from the nonthermal Cu enabled by increasing gas rarefaction. The increasing nonthermal flux then tends to moderate the ionization fraction.

The ability to fill trenches results from an interplay between the angular distribution, the ionization fraction of the incident flux, and the aspect ratio of the feature. For example, profiles are shown in Fig. 15 at 40 mTorr, 0.3 kW magnetron power, 1.0 kW ICP power for dc substrate biases of −25, −12, and 0 V. As the magnitude of the dc bias decreases, the energy of the incident ions decreases and their angular distribution broadens. The ion energy and angular distributions at −12 and 0 V substrate biases are similar to Fig. 6(a), except for being lower in energy and broader in angle. For example, the incident energy distribution at 0 V is between 20 and 50 eV, and the angular distribution is broader, up to 20°. As a result, less resputtering of the overhanging deposits occurs at the lower bias. The broader angular distribution of the ions also contributes an increasing flux to the larger solid angle viewed at the top of the trench. As a result, pinch-off occurs.

The ability to fill features at a given set of operating conditions also depends on the aspect ratio of the feature. For example, deposition profiles for feature aspect ratios of 1.1, 2, 3, and 4 are shown in Fig. 16. At 40 mTorr, 0.3 kW

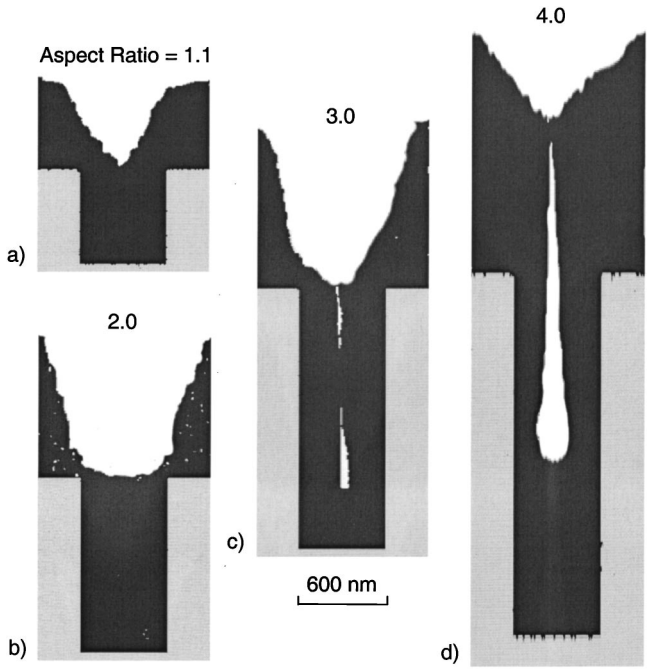

FIG. 16. Deposition profiles for different aspect ratios at 40 mTorr, 0.3 kW magnetron, 1.0 kW ICP, and −25 V dc bias on the substrate. Complete filling is not achieved for aspect ratios greater than 3.

magnetron power and 1.0 kW ICP, filling occurs only for the aspect ratios of 1.1 and 2. A void occurs at an aspect ratio of 3, which grows larger as the aspect ratio increases to 4. The minimum ionization fraction required to fill a trench without voids as a function of aspect ratio is shown in Fig. 17. The ionization fraction in Fig. 17 was increased by increasing pressure. As the aspect ratio of the trench increases, the fraction of the neutral fluxes that are able to reach the bottom of the trench decreases due to the broader angular distribution of the neutrals and their nonzero sticking coefficient. Ions are able to penetrate deeper into the trench with their narrower angular distribution. Ions also sputter overhanging deposits which keep the top of the trench open for a longer period. As a result, the ionization fraction required for complete filling increases with the aspect ratio. These results indicate that the largest aspect ratio which can be completely filled in this geometry is 3 where the ionization fraction is about 0.86. It is difficult to exceed an ionization fraction of 0.9 due to rarefaction of the gas which occurs at high power loading.[9,19,20] The rarefaction reduces the rate of sputtered atom thermalization, similar to operating at lower pressure, thus limiting the ionization rate. These results require that the energy of the incident ions is sufficiently low that sputtering at the bottom of the trench does not dominate over deposition. For example, the results of Vyvoda *et al.* showed that the bottom coverage was significantly reduced by sputtering due to the ions at 175 eV.[8]

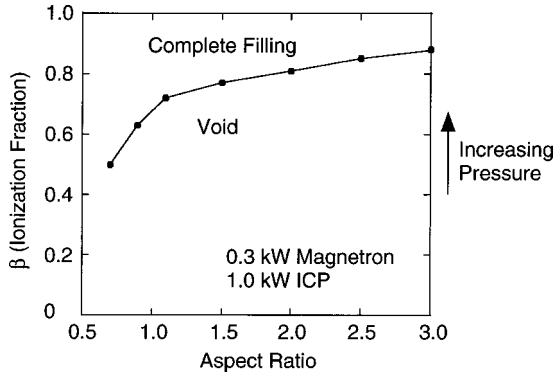

FIG. 17. Minimum ionization fraction of the incident metal flux required for complete filling as a function of aspect ratio for 0.3 kW magnetron, 1.0 kW ICP, and −25 V dc bias on the substrate. The required ionization fraction increases with the aspect ratio due to the inability of the neutral flux to reach the bottom of the trench. The ionization fraction was changed by varying pressure.

V. CONCLUDING REMARKS

An integrated plasma equipment and feature scale model has been developed and applied to trench filling using IMPVD. The model self-consistently accounts for the magnitude, the angular distribution, and the energy distribution of the incident metal flux. The predicted trench profiles agree with experimentally observed trends. The incident ions are predicted to have broadened energy and angular distributions, due to oscillation of the plasma potential induced by the rf voltage on the coils immersed in the plasma and collisions in the presheath, respectively. Surface diffusion is beneficial to conformal deposition of Cu. The perturbation of the radial electric field at the wafer edge may produce an asymmetric angular distribution of the incident flux, and consequently an asymmetry in the metal deposit in the trench. The model predictions indicate that the ionization fraction of the depositing metal flux is the critical factor in trench filling. Formation of voids occurs when the ionization fraction of the incident metal flux is too low. As the aspect ratio of the trench increases, the required ionization fraction for complete trench filling also increases. High pressure, low magnetron power, and high ICP power are the operating conditions which maximize the ionization fraction.

ACKNOWLEDGMENT

This work was funded by Semiconductor Research Corporation, NSF (CTS99-74962), DARPA/AFOSR, and Applied Materials Inc.

[1]K. Lee, Solid State Technol. **41**, 85 (1998).
[2]J. Hopwood, Phys. Plasmas **5**, 1624 (1998).
[3]J. A. Cunningham, Semicond. Int. **23**, 97 (2000).
[4]S. M. Rossnagel and J. Hopwood, J. Vac. Sci. Technol. B **12**, 449 (1994).
[5]S. M. Rossnagel, J. Vac. Sci. Technol. B **16**, 2585 (1998).
[6]S. Hamaguchi and S. M. Rossnagel, J. Vac. Sci. Technol. B **13**, 183 (1995).
[7]P. F. Cheng, S. M. Rossnagel, and D. N. Ruzic, J. Vac. Sci. Technol. B **13**, 203 (1995).
[8]M. A. Vyvoda, C. F. Abrams, and D. B. Graves, IEEE Trans. Plasma Sci. **27**, 1433 (1999).
[9]J. Lu and M. J. Kushner, J. Appl. Phys. **87**, 7198 (2000).
[10]R. J. Hoekstra, M. J. Grapperhaus, and M. J. Kushner, J. Vac. Sci. Technol. A **15**, 1913 (1997).
[11]J. Lu and M. J. Kushner, J. Appl. Phys. **89**, 878 (2001).
[12]H. Wei, Z. Liu, and K. Yao, Vacuum **52**, 435 (1999).

[13]M. J. Grapperhaus, Z. Krivokapic, and M. J. Kushner, J. Appl. Phys. **83**, 35 (1998).
[14]N. Masunami, Y. Yamamura, Y. Itikawa, N. Itoh, S. Kazumata, S. Miyagawa, K. Morita, R. Shimizu, and H. Tawara, At. Data Nucl. Data Tables **31**, 1 (1984).
[15]R. A. Powell and S. Rossnagel, Thin Films **26**, 27 (1999).
[16]D. E. Hanson, A. F. Voter, and J. D. Kress, J. Appl. Phys. **82**, 3552 (1997).
[17]J. D. Kress, D. E. Hanson, A. F. Voter, C. L. Liu, X. Y. Liu, and D. G. Coronell, J. Vac. Sci. Technol. A **17**, 2819 (1999).
[18]K. Suzuki, K. Konishi, N. Nakamura, and H. Sugai, Plasma Sources Sci. Technol. **9**, 199 (2000).
[19]S. M. Rossnagel, J. Vac. Sci. Technol. A **6**, 19 (1988); J. Vac. Sci. Technol. B **16**, 3008 (1998).
[20]Y. Andrew, J. H. Booske, S. Lu, T. G. Snodgrass, and A. E. Wendt, Plasma Sources Sci. Technol. **9**, 562 (2000).